Atom Vacancies on a Carbon Nanotube: To What Extent Can We Simulate their Effects?

Jaap M. H. Kroes,[†] Fabio Pietrucci,[†,§] Adri C. T. van Duin,[‡] and Wanda Andreoni*[,†]

[†]Institut de Théorie des Phénomènes Physiques, Ecole Polytechnique Fédérale de Lausanne, 1015 Lausanne, Switzerland

[‡]Department of Mechanical and Nuclear Engineering, The Pennsylvania State University, University Park, Pennsylvania 16802, United States

S Supporting Information

ABSTRACT: Atom vacancies are intrinsic defects of carbon nanotubes. Using a zigzag nanotube as reference, this paper focuses on the comparison of calculations performed within density functional theory and a number of classical force fields widely used for carbon systems. The results refer to single and double vacancies and, in particular, to the induced structural changes, the formation energies, and the energy barriers relative to elementary processes such as reconstruction, migration, and coalescence. Characterization of these processes is remarkably different in the different approaches. These findings are meant to contribute to the construction of DFT-based classical schemes for carbon nanostructures.
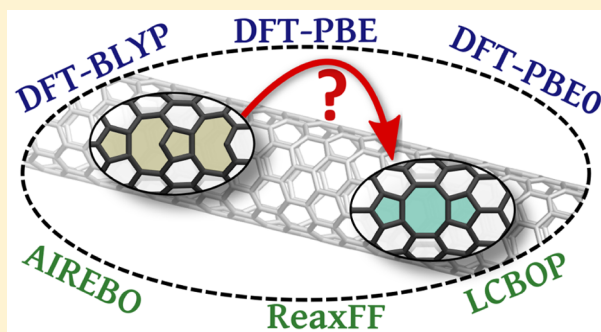
1. INTRODUCTION

Vacancies, interstitials, bond-rotations, and nonhexagonal rings are common intrinsic defects of graphitic surfaces in general. Pristine carbon nanotubes (CNTs) are not immune from defects[1] although they are often described as defect-free to a large extent. Moreover, given the reduced dimensionality of a nanotube, a single defect is expected to have stronger effects on its physical and chemical properties than on graphite or also graphene. This explains the great interest in identifying defects on nanotubes also at very low concentration, and even in engineering defected single-wall CNTs so as to tailor their electronic properties.[2,3] Although several techniques are able to detect the presence of point defects,[1,4−6] identifying their nature remains a very challenging task and requires a combination of experimental data with modeling and calculations (see, e.g., ref 7).

In particular, we refer here to atomic vacancies. They are not expected to form at high concentration during synthesis of carbon nanotubes, although taking place at temperatures of the order of 3000 °C, but in postsynthesis processes.[1] Systematic studies have required their artificial generation from irradiation with high-energy electrons or ions.[8,9] The role of vacancies, however, is often invoked to explain the chemical behavior of nonartificially defected nanotubes, e.g., to rationalize the anomalously strong binding of molecules like NO_2[10] or to characterize oxidation processes[11,12] or to account for the coalescence of single-wall nanotubes.[13] Coalescence of vacancies in large voids is another interesting phenomenon, which has been observed in CNTs (see, e.g., ref 14), in analogy with graphite and graphene.

Therefore, a model of realistic systems based on carbon nanotubes cannot ignore the presence of defects such as vacancies. No systematic work exists on CNTs with vacancies, namely on the fate of the latter and their effects. Still, several calculations based on density functional theory (DFT) have been published on small-diameter (0.5−1 nm) CNTs, aimed at establishing the thermodynamically favored configurations of single (SV) and double (DV) vacancies and their formation energies,[15−21] and a few studies have appeared aiming at understanding how they might modify the characteristics of the pristine nanotube[12,22,23] or how their presence might manifest itself, e.g., in Raman spectra.[7] On the other hand, for the simulation of growth or fracture or other disruptive processes, where atoms may be desorbed and reabsorbed, knowledge so far relies on classical schemes.[24−29] Still, the latter do not provide sufficient characterization of either most probable configurations or the mechanisms underlying dynamical processes. Moreover, only few attempts have been made to compare classical and quantum-mechanical description of defective structures of graphitic surfaces.[19,30]

The aim of this paper is twofold: (i) to compare the predictions of commonly used carbon force-fields to those of DFT calculations and (ii) within DFT to investigate the dependence of the results on the exchange-correlation (xc) functional. In particular, for the latter, we are interested in identifying the changes induced by introducing partial effects of the exact exchange on passing from a gradient-corrected xc functional to a hybrid one. The physical quantities we consider

are formation energies, structural characteristics, and energy barriers associated with reconstruction, migration, and vacancy coalescence. As working example, we consider the (10,0) zigzag nanotube. This choice allows us also comparison with previous DFT calculations, with which a global agreement is found.

2. METHODS AND MODELS

We report the results of calculations on the (10,0) zigzag nanotube with single and double vacancies, using DFT-based schemes and also diverse force fields. For the former, we performed spin-polarized (unrestricted) calculations within the PBE[31] and the BLYP[32] approximations for the exchange-correlation functionals, and the plane-wave pseudopotential[33] scheme, as implemented in the CPMD code.[34] Part of the calculations were repeated within the hybrid PBE0[35] exchange-correlation functionals. Only spin states of the lowest multiplicity (singlets) are considered. Details are the same as in our previous papers.[36] More can be found in the Supporting Information (SI).

As classical interatomic potentials, we used the Adaptive-Intermolecular-Reactive-Empirical-Bond-Order (AIREBO),[37] the Long-range Carbon Bond-order Potential (LCBOP),[38] and ReaxFF[39] force fields. For the sake of comparison, the outcome of Reactive-Empirical-Bond-Order (REBO)[40] is given in the SI. Of the two available versions of LCBOP, we report here our complete results obtained with the LCBOPI[38] and partial ones for the LCBOPII[41] in the SI. As for the ReaxFF, we refer to the latest version (ReaxFF15[42]) that was successfully applied to condensed as well as molecular phases such as fullerenes. Our findings with other versions,[43,44] previously applied to carbon systems, are also given in the SI. For the sake of comparison, we also discuss some results obtained with the Tersoff potential,[45] originally proposed for amorphous carbon, and reported in the SI.

Atomistic models of 359 or 358 atoms are used, in periodically repeated tetragonal cells with parameters corresponding to the equilibrium of the 360-atom system (see SI). Only the $k = 0$ point of the Brillouin zone (BZ) is considered. This size was decided on the basis of the convergence of the formation energy. This is shown in Figure 1 for a few vacancy configurations in PBE and ReaxFF15, and in Figure S1 for the other classical potentials. Only for the 5r8r5r-Z structure of the DV, calculations reach convergence slowly both in the DFT and the classical schemes here applied. Therefore, all the results

reported below for the 5r8r5r-Z DV refer to a model of 598 atoms, for which convergence is attained within 1%. As will be shown in section 3, this behavior reflects the relatively longer range of the perturbation induced by removing two atoms sharing a zigzag bond. On the other hand, in the case of the short-range Tersoff potential, convergence is attained more easily also in the case of the 5r8r5r-Z DV (within less than 1% for a 358-atom cell).

The vacancy formation energy E_f is defined as

$$E_f = E_{vac} + n\mu - E_0$$

where n is the number of missing atoms, E_{vac} and E_0 are the total energies of the defective and pristine nanotubes respectively, and μ is the chemical potential of carbon. The latter should be referred to the most stable carbon structure. In general, however, its value is approximated by the energy per atom in the pristine nanotube: $\mu = E_0/N$.

For the study of activated processes and the estimate of energy barriers, we apply the nudged-elastic-band (NEB) method.[46] In the simulations using force-fields, vibrational analysis was employed to characterize local minima and transition states. Note that the barriers relative to the PBE0 xc functional were evaluated along the PBE path.

In the following we will mention some of the previous calculations for comparison with ours. In particular, the selected calculations also use periodic boundary conditions and gradient-corrected xc functionals. The details in Table S1 help in understanding the possible differences reported below. Most of these calculations use smaller unit cells than those of our model, but augmented with a coarse sampling of the BZ beyond $k = 0$. Therefore, the structural relaxation beyond the 120- or 240-atom cell, is ignored. This is the main difference with our representation of the CNT, that allows for such a relaxation to a larger extent and for an analysis of its relevance.

Moreover, in order to represent highly diluted defects, the cell size must be chosen sufficiently large so as to avoid spurious effects of their interaction. This same issue was first emphasized in previous work on hydrogen and oxygen chemisorption on CNTs.[36] As pointed out in ref 47, as a consequence of the periodic boundary conditions, possible torsional deformations of the tube induced by the defects will be limited to those compatible with the symmetry of the supercell. However, in general, tube deformations are likely to be weak for the cases of highly diluted defects that our supercells are meant to represent.

3. STRUCTURAL PROPERTIES AND FORMATION ENERGIES

In order to explore a larger set of geometries than those sporadically considered in the literature, the starting step of our investigation consisted of classical molecular dynamics simulations (using AIREBO) of a large-size model for the nanotube (~100 000 atoms ~1 μm length), run at high temperature (up to 2500 K) for several concentrations and followed by simulated annealing. We selected the vacancy configurations with higher population and optimized their structure ab initio. Eventually, however, only a few could be classified as local minima of either the DFT-PBE or the DFT-BLYP potential energy surfaces. These are shown in Figures 2 and 3. Geometries denoted as 12r and 14r are plotted as reference and represent the holes generated by stripping one or two atoms, thus leaving three or four DBs.
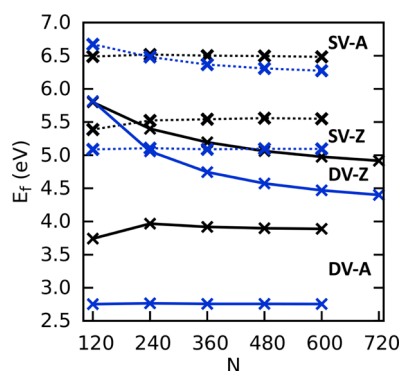
Figure 1. CNT:(10,0): Formation energies calculated for different sizes of the periodically repeated unit cell. N is the number of atoms in the periodically repeated unit cell of the pristine nanotube. (black crosses) PBE; (blue crosses) ReaxFF15.
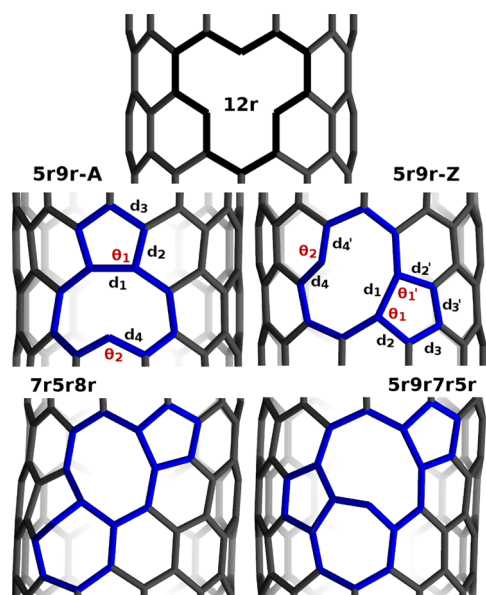
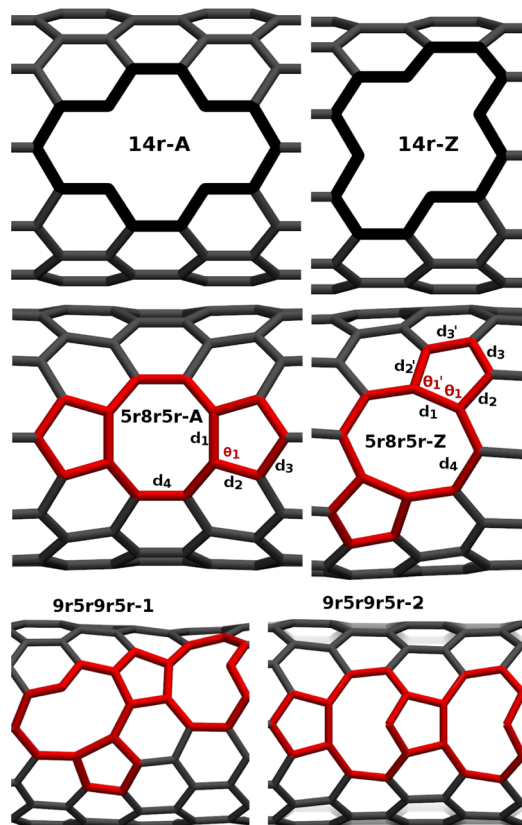**Figure 2.** CNT:(10,0): Configurations with a single vacancy (SV).

Figure 3. CNT:(10,0): Configurations with a double vacancy (DV).

Our results for the formation energies E_f are given in Tables 1 and 2, also compared with previous calculations. In agreement with refs 17 and 18, we find that the configurations with the lowest formation energies have one (SV) or two (DV) strained pentagons and a nine- or eight-membered ring for the SV and the DV respectively. In the following we shall denote these structures as SV-A(Z) and DV-A(Z). Double-vacancies in the 5r9r5r9r-1 and 5r9r5r9r-2 geometries comprehend two adjacent single-vacancies, namely SV(A)+SV(Z) and two

Table 1. Single Vacancy Formation Energies E_f (eV)[a]

	12r	5r9r-A	5r9r-Z	5r5r/ 9r9r	5r9r7r5r	7r5r8r
PBE	×	5.5	6.5	×	7.9	9.5
BLYP	×	5.5	6.3	×	7.5	9.1
PBE0	×	6.0 [6.1]	7.1 [7.2]	×		
PW[15]	7.4	5.5	6.7			
PBE[17]	×	(5.67[a]) 5.65[b]	7.1	×		
PW[18]	×	5.5[c], 6.5[d]		×		
ReaxFF	7.7	5.1	6.4	5.4	7.0	7.1
AIREBO	6.7	4.9	5.9	4.45	7.6	7.4
LCBOPI	7.1	4.6	5.8	5.7	7.1	7.3

[a] a and b differ in the size of the unit cell; c and d in the algorithm implementation (see Supporting Information Table S1.) For PBE0, we report in parentheses the values obtained in the PBE geometry. × = unstable.

SV(A)s, respectively. Comparison of the E_f values shows a negligible difference with the isolated SVs and, thus, no tendency to cluster.

As shown in Tables 1 and 2, PBE and BLYP functionals are in close agreement regarding the values of the formation energies and in most cases, BLYP tends to reduce them. Adding part of the exact exchange as in the PBE0 functional increases E_f significantly but preserves the ranking. The same conclusions can be derived from Table 3 where the energy gain is reported, relative to the original 12r and 14r structures. We have also verified that including Grimme's corrections[48] for van der Waals interactions has no appreciable effect. Moreover, we verified the effect of the inclusion of spin-polarization on the values of the formation energies: it is relevant—decrease of E_f by 0.3 eV—only for the SV(Z) configuration, both isolated and in the 5r9r5r9r-1 configuration.

Reference 15 apparently found the 12r geometry to correspond to a local energy minimum, in analogy with other LSDA computations.[16] Apart from this case, there is a global consistency among all GGA calculations.

We remark that the geometrical changes from PBE to BLYP and from PBE to PBE0 are very small, i.e. less than 1%. In particular, as shown in Tables 1 and 2, the latter lead to a change of the formation energies of at most 2%. These results justify the approximation we make in section 4 where we estimate the PBE0 energy barriers using the NEB path formed by the PBE images.

We now turn to the comparison of our DFT and force-field calculations. We refer again to Tables 1–3 and also Tables S1–S3. As mentioned in section 2, the case of the original Tersoff potential is considered separately.

There is full agreement in the prediction that formation energies of double vacancies are significantly lower than those of monoatomic vacancies. Large holes are in general disfavored and a certain consistency is found in the ranking of the geometries corresponding to the DFT local minima, especially for ReaxFF15.

However, a few remarkable differences are recognized, and especially: (i) Nonreconstructed geometries with 12-fold and 14-fold rings (12r and 14r) are unstable in DFT but are local minima in all force fields here applied. (ii) Most potentials of the REBO family—as already pointed out in ref 19—predict a configuration with two adjacent 5-membered rings (5r5r in Figure 4) as the ground state. This structure also corresponds to a local minimum of the potential energy surface of the

Table 2. Double Vacancy Formation Energies E_f (eV)^a

	14r-A	14r-Z	5r8r5r-A	5r8r5r-Z	9r5r9r5r-1	9r5r9r5r-2
PBE	×	×	3.9	5.0	12.0	11.1
BLYP	×	×	4.0	4.8	11.6	10.93
PBE0	×	×	4.3 [4.3]	6.0 [6.0]	13.6 [13.85]	
PBE[17]			(3.90^a) 4.06^b	6.65		
PW[18]	×	×	3.5^c, 4.2^d			
PBE[49]			3.61	6.07		
ReaxFF	9.8	10.15	2.8	4.4	10.85	9.3
AIREBO	8.9	9.1	4.3	6.1	10.5	9.8
LCBOPI	9.2	9.5	3.2	5.2	10.2	9.3

^{a} a and b differ in the size of the unit cell; c and d in the algorithm implementation (see Supporting Information Table S1.) For PBE0, we report in parentheses the values obtained in the PBE geometry. × = unstable.

Table 3. Energy Gain Corresponding to Metastable and Stable Structures, Relative to the Pristine Nanotube with One or Two Atoms Removed^a

	12r	5r9r-A	5r9r-Z	5r5r/9r9r	14r-A	14r-Z	5r8r5r-A	5r8r5r-Z
PBE	×	2.32	1.36	×	×	×	5.59	4.59
BLYP	×	2.08	1.29	×	×	×	5.09	4.32
PBE0	×	2.62	1.41	×	×	×	6.10	4.41
ReaxFF	3.71	6.34	5.07	6.04	5.03	5.04	12.12	10.80
AIREBO	0.91	2.75	1.69	3.17	1.28	1.11	5.92	4.07
LCBOPI	0.91	3.39	2.21	2.31	1.20	0.90	7.22	5.20

^{a} 12r and 14r are the geometries obtained after structural relaxation in the classical potential schemes. × = unstable.
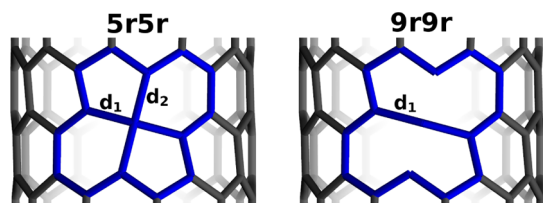

Figure 4. Single vacancy: two additional geometries corresponding to stable or metastable states of the force fields (see text).

ReaxFF15 but is unstable in our DFT calculations. With reference to Figure 4, the pair of distances $(d_1; d_2)$ are $(1.52; 1.61)$ Å in ReaxFF15 and $(1.64; 1.70)$ Å in AIREBO. In LCBOPI, a local energy minimum is found for a similar structure with $d_1 = 1.46$ Å and $d_2 = 1.93$ Å. Thus, it can be better described as one with two adjacent 9-membered rings (9r9r in Figure 4). We recall that the LSDA calculations of ref 16 predict that this type of configuration—corresponding to full saturation of the three dangling bonds—is metastable and only 0.5 eV higher than the ground state (5r9r-A).

The strain induced by the presence of vacancies can be represented by the map of the atom displacements along the nanotube, as in Figure 5 for PBE and ReaxFF15. These plots confirm that, as mentioned in ref 2, the range of the perturbation induced by atom loss depends on the specific configuration and in particular suggest why the Z-structures are less energetically favored. The largest displacements amount to 0.6−0.7 Å in both PBE and RexFF15 schemes. The other force fields exhibit the same qualitative behavior. However, e.g. in the LCBOPI and AIREBO descriptions, displacements can reach 0.9−1 Å in the case of the SV-Z (see Figures 1 and 2 of the SI). Inspection of the structural changes at and around the nonhexagonal rings—as reported in Tables 4 and 5—reveals further similarities and differences. A remarkable discrepancy can be identified in the DV-Z configuration of ReaxFF15, namely the θ_2 value which reflects the flatness of the 9-

membered ring. Also, in the quantum-mechanical approaches, the new bonds generated in the defect reconstruction are much weaker than the graphitic ones. The AIREBO and LCBOPI force fields show this same behavior.

As shown in Tables S1 and S3, the results obtained with the original Tersoff potential are at odds with the scenario just described. Formation energies are at least 2 eV higher, double-vacancies are not more easily formed than single vacancies. Moreover, for the single vacancies, the 12r-A and 12r-Z unreconstructed geometries are favored and the pentagonal rings emerging from the reconstructions, if any, have weaker bonds.

The Tersoff potential is often considered an example of a simple coordination-dependent and short-range interaction scheme. However, not only the range of the interactions is important in the construction of a classical potential, but also the selection of the analytic form, the type and number of parameters included in the fitting and the specific test cases on which the parametrization is built on. The diversity of the strategies followed in the construction of the different force fields examined here does not allow for a clear understanding of the differences found in the results.

4. ACTIVATED PROCESSES

Here we focus on the description of some processes accompanying or following the formation of mono- and double-vacancies. The results below will show that there are important differences among the scenarios provided by the different approaches here applied, and especially between the quantum and the classical approaches. Calculations refer to the 359- or 358-atom unit cells.

4.1. Reconstruction. As we clarified above, in our ab initio calculations the 12r and 14r structures, generated by removal of one or two atoms from the pristine CNT, spontaneously reconstruct. As an example, Figure 6 illustrates the progress of one of our geometry optimizations, leading to the 5r9r-Z. The
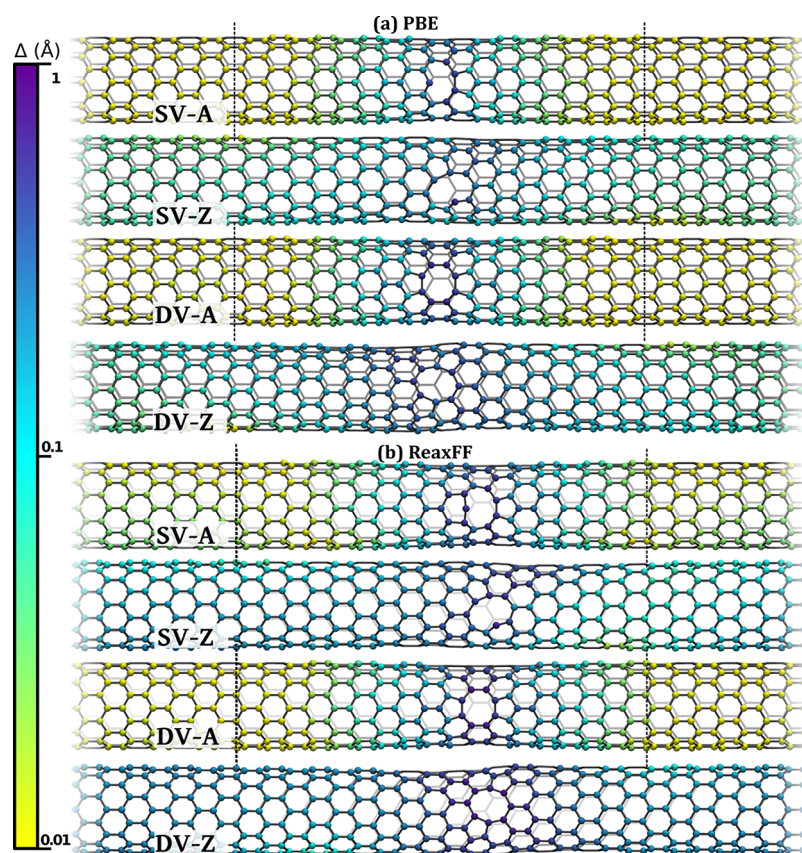
Figure 5. Displacements (Å) of the carbon positions induced by SVs and DVs: (a) PBE; (b) ReaxFF15.

Table 4. Single Vacancy Configurations[a]

5r9r-A	d_1	d_2	d_3	θ_1	d_4	θ_2
PBE	1.54	1.44	1.41	105	1.39	116
BLYP	1.55	1.44	1.42	105	1.39	116
PBE0	1.54	1.43	1.41	105	1.37	117
ReaxFF	1.45	1.43	1.40	106	1.39	160
AIREBO	1.47	1.46	1.42	107	1.41	117
LCBOPI	1.48	1.47	1.43	106	1.41	119
5r9r-Z	d_1	$d_2;d_2'$	$d_3;d_3'$	$\theta_1;\theta_1'$	$d_4;d_4'$	θ_2
PBE	1.68	1.45;1.43	1.41;1.40	104;100	1.37;1.36	124
BLYP	1.70	1.45;1.43	1.41;1.40	103;100	1.38;1.36	124
PBE0	1.70	1.43;1.42	1.40;1.40	104;99	1.37;1.35	125
ReaxFF	1.48	1.44;1.43	1.39;1.39	107;100	1.31;1.31	155
AIREBO	1.66	1.46;1.48	1.40;1.39	105;98	1.40;1.40	117
LCBOPI	1.60	1.50; 1.50	1.42; 1.41	105; 101	1.40; 1.40	121

[a]Bond distances (d_i) are in angstroms, and angles are in degrees.

plateau corresponds to the 12r geometry after mere relaxation, which implies only a small increase of the δ_3 distance and amounts to a gain of ∼0.5 eV. Landing into the local minimum is clearly barrierless and is accompanied by the formation of a new (although relatively weak) bond.

On the contrary, in all the classical potential schemes we have considered, this process requires a high energy barrier (of the order of 1 ev) both for the SV and the DV—as shown in Table 6—and develops through a two-step path for the DV, each related to the formation of a 5-membered ring.

Indeed, structural reconstruction after atom removal is driven by the tendency to saturate dangling bonds via the formation of new bonds but is opposed by as a strain increase in the carbon network. The former is facilitated by orbital rehybridization, namely a process which is not present in a classical description. Therefore, in order to overcome the latter, a more complicated process is needed to land into a structure with higher coordination.

4.2. Migration of a Single Vacancy. We considered the transformation from the 5r9r-Z to the 5r9r-A structure. The DFT-GGA approaches predict a concerted mechanism, namely a bond switching taking place smoothly as a single step, with a barrier of about 0.6 eV (Table 7). This is described in Figure 7, where the variation of specific distances is plotted. This shows that the dissolution of the five-membered ring in 5r9r-Z is accompanied by the formation of another in 5r9r-A. On the

Table 5. Double Vacancy Configurations[a]

5r8r5r-A	d_1	d_2	d_3	d_4
PBE	1.50	1.42	1.42	1.46
BLYP	1.51	1.43	1.42	1.46
PBE0	1.50	1.42	1.41	1.46
ReaxFF	1.44	1.43	1.40	1.42
AIREBO	1.44	1.45	1.42	1.40
LCBOPI	1.45	1.47	1.44	1.42
5r8r5r-Z	d_1	$d_2;d_2'$	$d_3;d_3'$	d_4
PBE	1.58	1.44;1.43	1.41;1.40	1.48
BLYP	1.59	1.45;1.43	1.41;1.40	1.48
PBE0	1.59	1.44;1.42	1.40;1.40	1.48
ReaxFF	1.47	1.44;1.43	1.39;1.38	1.44
AIREBO	1.55	1.46;1.47	1.41;1.40	1.43
LCBOPI	1.54	1.48;1.48	1.42;1.41	1.44

[a]Geometric characteristics as in Table 4. The values of the bond angles are the same in each scheme (A: $\theta_1 = 106°-107°$. Z: $\theta_1 = 105°-106°$; $\theta_1' = 102°-103°$.).
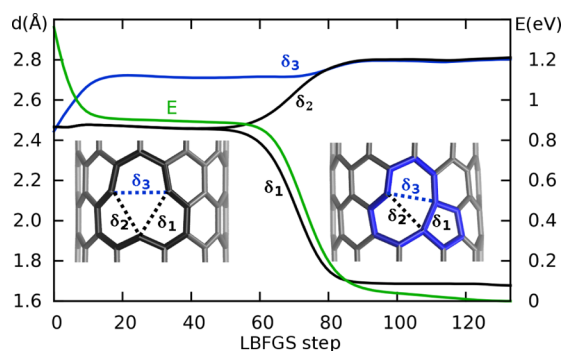

Figure 6. Geometry optimization—using the LBFGS algorithm[50]—starting from the pristine nanotube after loss of one atom.

Table 6. Force Fields: Energy barriers (eV) for Defect Reconstruction on the (10,0)−CNT[a]

force field	R(5r9r-A)	R(5r9r-Z)	R(5r8r5r-A)	R(5r8r5r-Z)
ReaxFF15	1.2	1.4	1.1;0.6	0.6;0.5
AIREBO	1.1	1.3	1.4;0.6	1.0;0.8
REBO	1.0	1.2	1.2;0.4	0.9;0.4
LCBOPI	1.3	1.0	1.1;0.1	0.9;0.7

[a]The double-vacancy reconstruction consists of two successive steps, each corresponding to the formation of one bond. In our DFT calculations, these reconstructions are barrierless.

Table 7. Energy Barriers (eV) for Single Vacancy Migration from the 5r9r-Z to the 5r9r-A Structure[a]

PBE	0.65
BLYP	0.6
PBE0	0.7
PW[18]	0.45
ReaxFF15	**1.2**;1.1
LCBOPI	**1.3**;0.3

[a]For the classical potentials there are two barriers with the 9r9r structure as intermediate state; the highest barrier is highlighted.

contrary, ReaxFF15 and LCBOPI predict that this transition takes place in two steps through an intermediate corresponding to the 9r9r configuration (Figure 4). As mentioned above, the latter is the ground state in both AIREBO and REBO
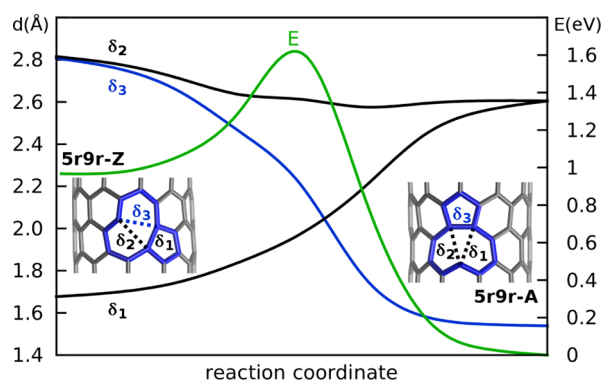

Figure 7. Distance variation along the transformation from the 5r9r-Z to the 5r9r-A structure. Note that in the former δ_1 corresponds to d_1 in Table 4 and in the latter δ_3 corresponds to d_1 in Table 4.

approaches. The transformations from the 5r9r-Z and the 5r9r-A configurations to the 9r9r are also non spontaneous, and require barriers of the order of 1 eV.

4.3. Coalescence of Two Single Vacancies. Starting from two SVs, both in the 5r9r-A configuration, we simulated their coalescence in a DV 5r8r5r-A.

The PBE and BLYP paths coincide and involve two steps (in Figure 8): the first one corresponds to a low barrier (∼0.1 eV; Table 8) and consists of a bond switch (from C1−C3 to C1−
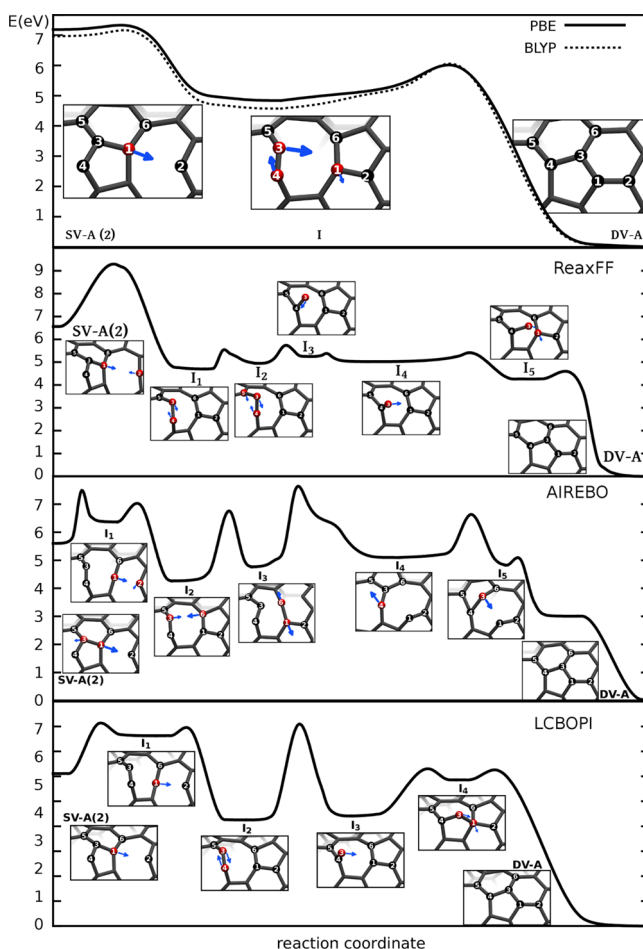

Figure 8. Coalescence of two monovacancies into a double-vacancy from NEB simulations.

Table 8. Energy Barriers (eV) for the Coalescence of Two Aligned Single Vacancies (Both 5r9r-A as in 9r5r9r5r-2) into a Double Vacancy (5r8r5r-A)[a]

	B1	B2	B3	B4	B5	B6
PBE	0.1	**1.15**				
BLYP	0.1	**1.4**				
PBE0	0.2	**1.1**				
	B1	B2	B3	B4	B5	B6
ReaxFF	**3.0**	0.8	0.8	0.1	0.5	0.5
AIREBO	1.9	0.5	2.5	**2.7**	1.5	0.2
LCBOPI	2.1	0.2	**3.8**	1.9	0.4	

[a]The highest barrier is highlighted.

C2) leading to the migration of a 5-membered ring in the intermediate (I ; with an energy lowering of 2.3 eV) still including two under-coordinated atoms; the second step requires a much higher barrier (~1 eV; Table 8) and leads to a further pentagon migration and the formation of two new bonds, thus recovering a three-coordinated network (and gaining almost 9 eV). No significant difference is found in the values of the energy barriers between PBE and BLYP.

Unlike DFT-GGA, the force-fields predict rugged energy profiles, going through several steps, and higher energy barriers. The results of the ReaxFF15 simulation are shown in Figure 8. The first step is the same observed in the GGA simulations, namely the bond-switch leading to the same type of intermediate (I1); however, it involves a much higher barrier (~3 eV; Table 8) and is the diffusion-limiting step of the coalescence process. The latter goes then through a series of local readjustments with barriers up to 0.8 eV (Table 8).

In both AIREBO and LCBOPI simulations (Figure 8), bond breaking (with a ~2 eV barrier) and bond formation are not concerted and involve short chains. Even higher barriers characterize the subsequent rearrangements of the structure (Table 8). The AIREBO pathway includes the formation of other defects like a three-membered ring and the 9r9r configuration; whereas, the LCBOPI path includes atom protrusions and self-healing.

5. CONCLUSIONS

The description of the physical chemistry of CNTs may depend on the theoretical and numerical algorithm adopted. Here we have analyzed this dependence in the case of a zigzag nanotube with single and double vacancies. Beyond recognizing some static properties on which there is agreement among different—both ab initio and classical—schemes, the present study has shown and emphasized the difficulties that current classical algorithms encounter in describing and quantitatively assessing the evolution of common processes following the desorption of a few atoms from a carbon nanotube.

On one hand, we find a close agreement between the results obtained with the DFT-GGA functionals PBE and BLYP as already pointed out in the study of hydrogen and oxygen chemisorption.[36] Also the partial addition of exact exchange, as in the PBE0 functional, has a negligible effect on the structural characteristics and the ranking of the different vacancy configurations considered here. Still, it increases the formation energies significantly. Consensus is found in general on the values of the energy barriers estimated for a few relevant transformations.

On the other hand, we find remarkable discrepancies between the results of quantum-mechanical and the classical

schemes here examined. For example, contrary to the well-known tendency of carbon aggregates to avoid dangling bonds and thus spontaneously removing them through rebonding, unreconstructed structures are not unstable in the classical approaches. They correspond to metastable states separated by high-energy barriers from the low-energy geometries. Also the examples we have studied of the migration and coalescence of single vacancies consistently confirm that in the classical description vacancies have much lower mobility than predicted by DFT-GGA calculations. Moreover, our findings reveal areas of the classical potential-energy surface with pronounced roughness compared to DFT-GGA.

Indeed bond-formation and bond-breaking are intrinsically quantum events but the corresponding energy loss or gain can be obtained with force fields as result of the coordination decrease or increase. For example, the energetic preference for DVs over SVs and for the reconstructed over unreconstructed SVs is qualitatively reproduced in the classical approaches. However, the representation of the kinetic paths is much more complex. Indeed, transformations from one configuration to the other imply progressive changes in the electronic structure that are more complicated to simulate within a classical framework. Some care can and should still be taken on this issue so as to provide (at least) reasonable values for the potential-energy or free-energy barriers of relevant chemical and physical processes. For example, information on these quantities could be included either in the fitting or in the training sets used for the parametrization of the force field (see, e.g., ref 51 for a system other than carbon).

Simulations of carbon nanotubes—and more in general carbon nanostructures—of realistic sizes need the application of classical interatomic potentials. The present investigation shows that to ensure their reliability for defective structures an improvement is necessary that may require a systematic comparison with ab initio methods. In particular, consistency between force-field and DFT descriptions would allow for the construction of a combined quantum-classical (QM/MM) approach of controlled accuracy. In view of the importance of carbon nanotubes as components of diverse technologies and the continuous progress in their applications (see, e.g., refs 52−54), we believe that this effort is worthwhile.

■ ASSOCIATED CONTENT

Ⓢ Supporting Information

Further details of the calculations and results obtained with other versions of the force fields considered here. All these results are cited in the main text. The Supporting Information is available free of charge on the ACS Publications website at DOI: 10.1021/acs.jctc.5b00292.

■ AUTHOR INFORMATION

Corresponding Author
*E-mail: wanda.andreoni@epfl.ch.

Present Address
§F.P.: Sorbonne Universités, UPMC University Paris 6, UMR 7590, IMPMC, 75005 Paris, France.

Notes
The authors declare no competing financial interest.

■ ACKNOWLEDGMENTS

■ REFERENCES

(1) Collins, P. G. In *Oxford Handbook of Nanoscience and Technology: Frontiers and Advances*; Narlikar, A., Fu, Y. E., Eds.; Oxford Univ. Press: Oxford, 2010; pp 35−107.

(2) Gómez-Navarro, C.; De Pablo, P. J.; Gómez-Herrero, J.; Biel, B.; Garcia-Vidal, F. J.; Rubio, A.; Flores, F. *Nat. Mater.* 2005, *4*, 534−539.

(3) Tolvanen, A.; Buchs, G.; Ruffieux, P.; Gröning, P.; Gröning, O.; Krasheninnikov, A. V. *Phys. Rev. B* 2009, *79*, 125430−125442.

(4) Dresselhaus, M.; Dresselhaus, G.; Jorio, A.; Souza Filho, A.; Saito, R. *Carbon* 2002, *40*, 2043−2061.

(5) Dresselhaus, M. S.; Dresselhaus, G.; Saito, R.; Jorio, A. *Phys. Rep.* 2005, *409*, 47−99.

(6) Hunt, S. R.; Fuller, E. J.; Corso, B. L.; Collins, P. G. *Phys. Rev. B* 2012, *85*, 235418−235428.

(7) Malola, S.; Häkkinen, H.; Koskinen, P. *Phys. Rev. B* 2008, *77*, 155412−155419.

(8) Krasheninnikov, A. V.; Nordlund, K. *J. Appl. Phys.* 2010, *107*, 071301−071372.

(9) Suzuki, S.; Yamaya, K.; Homma, Y.; Kobayashi, Y. *Carbon* 2010, *48*, 3211−3217.

(10) Mercuri, F.; Sgamellotti, A.; Valentini, L.; Armentano, I.; Kenny, J. M. *J. Phys. Chem. B* 2005, *109*, 13175−13179.

(11) Wang, C.; Zhou, G.; Wu, J.; Gu, B.-L.; Duan, W. *Appl. Phys. Lett.* 2006, *89*, 173130−173132.

(12) Liu, B.; Jiang, H.; Krasheninnikov, A. V.; Nasibulin, A. G.; Ren, W.; Liu, C.; Kauppinen, E. I.; Cheng, H.-M. *Small* 2013, *9*, 1379−1386.

(13) Terrones, M.; Terrones, H.; Banhart, F.; Charlier, J.-C.; Ajayan, P. M. *Science* 2000, *288*, 1226−1229.

(14) Jin, C.; Suenaga, K.; Iijima, S. *Nano Lett.* 2008, *8*, 1127−1130.

(15) Ma, Y.; Lehtinen, P. O.; Foster, A. S.; Nieminen, R. M. *New J. Phys.* 2004, *6*, 68−83.

(16) Berber, S.; Oshiyama, A. *Physica B: Condensed Matter* 2006, *376−377*, 272−275.

(17) Orellana, W.; Fuentealba, P. *Surf. Sci.* 2006, *600*, 4305−4309.

(18) Krasheninnikov, A.; Lehtinen, P.; Foster, A.; Nieminen, R. *Chem. Phys. Lett.* 2006, *418*, 132−136.

(19) Kotakoski, J.; Krasheninnikov, A. V.; Nordlund, K. *Phys. Rev. B* 2006, *74*, 245420−245424.

(20) Padilha, J. E.; Amorim, R. G.; Rocha, A. R.; da Silva, A. J. R.; Fazzio, A. *Solid State Commun.* 2011, *151*, 482−486.

(21) Lee, A. T.; Ryu, B.; Lee, I.-H.; Chang, K. J. *J. Phys.: Condens. Matter* 2014, *26*, 115303−115314.

(22) Santucci, S.; Picozzi, S.; Di Gregorio, F.; Lozzi, L.; Cantalini, C.; Valentini, L.; Kenny, J. M.; Delley, B. *J. Chem. Phys.* 2003, *119*, 10904−10910.

(23) Mielke, S. L.; Troya, D.; Zhang, S.; Li, J.-L.; Xiao, S.; Car, R.; Ruoff, R. S.; Schatz, G. C.; Belytschko, T. *Chem. Phys. Lett.* 2004, *390*, 413−420.

(24) Coluci, V. R.; Pugno, N. M.; Dantas, S. O.; Galvao, D. S.; Jorio, A. *Nanotechnology* 2007, *18*, 335702−335715.

(25) Okada, S.; Takagi, Y.; Kawai, T. *Jpn. J. Appl. Phys.* 2010, *49*, 02BB02−02BB05.

(26) Neyts, E. C.; Ostrikov, K.; Han, Z. J.; Kumar, S.; van Duin, A. C. T.; Bogaerts, A. *Phys. Rev. Lett.* 2013, *110*, 065501−065505.

(27) Zhang, X.; Jiang, J. *J. Phys. Chem. C* 2013, *117*, 18441−18447.

(28) Artyukhov, V. I.; Penev, E. S.; Yakobson, B. I. *Nat. Commun.* 2014, *5*, 4892−4897.

(29) Ozden, S.; Autreto, P. A. S.; Tiwary, C. S.; Khatiwada, S.; Machado, L.; Galvao, D. S.; Vajtai, R.; Barrera, E. V.; M. Ajayan, P. *Nano Lett.* 2014, *14*, 4131−4137.

(30) Krasheninnikov, A. V.; Nordlund, K.; Keinonen, J. *Phys. Rev. B* 2002, *65*, 165423.

(31) (a) Perdew, J. P.; Burke, K.; Ernzerhof, M. *Phys. Rev. Lett.* 1996, *77*, 3865−3868. (b) Perdew, J. P.; Burke, K.; Ernzerhof, M. *Phys. Rev. Lett.* 1998, *80*, 891−894.

(32) (a) Becke, A. D. *Phys. Rev. A* 1988, *38*, 3098−3100. (b) Lee, C.; Yang, W.; Parr, R. G. *Phys. Rev. B* 1988, *37*, 785−789.

(33) Troullier, N.; Martins, J. L. *Phys. Rev. B* 1991, *43*, 1993−2006.

(34) CPMD, IBM Corp. (1990−2015) and MPI für Festkörperforschung Stuttgart (1997−2001), http://www.cpmd.org.

(35) Adamo, C.; Barone, V. *J. Chem. Phys.* 1999, *110*, 6158−6170.

(36) (a) Andreoni, W.; Curioni, A.; Kroes, J. M. H.; Pietrucci, F.; Gröning, O. *J. Phys. Chem. C* 2012, *116*, 269−275. (b) Kroes, J. M. H.; Pietrucci, F.; Curioni, A.; Jaafar, R.; Gröning, O.; Andreoni, W. *J. Phys. Chem. C* 2013, *117*, 1948−1954. (c) Kroes, J. M. H.; Pietrucci, F.; Curioni, A.; Andreoni, W. *J. Chem. Theory Comput* 2014, *10*, 4672−4683.

(37) Stuart, S. J.; Tutein, A. B.; Harrison, J. A. *J. Chem. Phys.* 2000, *112*, 6472−6486.

(38) Los, J. H.; Fasolino, A. *Phys. Rev. B* 2003, *68*, 024107−024120.

(39) van Duin, A.; Dasgupta, S.; Lorant, F.; Goddard, W., III *J. Phys. Chem. A* 2001, *105*, 9396−9409.

(40) Brenner, D. W.; Shenderova, O. A.; Harrison, J. A.; Stuart, S. J.; Ni, B.; Sinnott, S. B. *J. Phys.: Condens. Matter* 2002, *14*, 783−802.

(41) Los, J. H.; Ghiringhelli, L. M.; Meijer, E. J.; Fasolino, A. *Phys. Rev. B* 2005, *72*, 214102−214115.

(42) Srinivasan, S. G.; van Duin, A. C. T.; Ganesh, P. *J. Phys. Chem. A* 2015, *119*, 571−580.

(43) Nielson, K.; van Duin, A.; Oxgaard, J.; Deng, W.-Q.; Goddard, W. A., III *J. Phys. Chem. A* 2005, *109*, 493−499.

(44) Chenoweth, K.; van Duin, A. C. T.; Goddard, W. A. *J. Phys. Chem. A* 2008, *112*, 1040−1053.

(45) Tersoff, J. *Phys. Rev. Lett.* 1988, *61*, 2879−2882.

(46) Mills, G.; Jonsson, H. *Phys. Rev. Lett.* 1994, *72*, 1124−1127.

(47) Zhang, D.-B.; James, R. D.; Dumitrica, T. *J. Chem. Phys.* 2009, *130*, 071101−071104.

(48) Grimme, S. *J. Comput. Chem.* 2006, *27*, 1787−1799.

(49) Saidi, W. A. *J. Phys. Chem. A* 2014, *118*, 7235−7241.

(50) Billeter, S. R.; Curioni, A.; Andreoni, W. *Computat. Mater. Sci.* 2003, *27*, 437−445.

(51) Hu, X. L.; Ciaglia, R.; Pietrucci, F.; Gallet, G. A.; Andreoni, W. *J. Phys. Chem. B* 2014, *118*, 6531−6538.

(52) Iannazzo, D.; Piperno, A.; Pistone, A.; Grassi, G.; Galvagno, S. *Curr. Med. Chem.* 2013, *20*, 1333−1354.

(53) Gong, T. A.; Maogang, S.; Xie, Y.; Bernardi, M.; Jasion, D.; Luck, K. A.; Marks, T. J.; Grossman, J. C.; Ren, S.; Hersam, M. C. *Nano Lett.* 2014, *14*, 5308−5314.

(54) Cao, Q.; Han, S.-j.; Penumatcha, A. V.; Frank, M. M.; Tulevski, J.; George, S.; Tersoff; Haensch, W. E. *ACS Nano* 2015, *9*, 1936−1944.